Intra-zero-energy Landau level crossings in bilayer graphene at high electric fields

Intra-zero-energy Landau level crossings in bilayer graphene at high electric fields

Feixiang Xiang,[*,†,‡] Abhay Gupta,[†,‡] Andrey Chaves,[*,¶,§] Zeb E. Krix,[†,‡] Kenji Watanabe,[‖] Takashi Taniguchi,[‖] Michael S. Fuhrer,[⊥] François M. Peeters,[§,¶] David Neilson,[§,‡] Milorad V. Milošević,[*,§,#] and Alexander R. Hamilton[*,†,‡]

†*School of Physics, University of New South Wales, Sydney, New South Wales 2052, Australia*

‡*ARC Centre of Excellence in Future Low-Energy Electronics Technologies, University of New South Wales, Sydney, New South Wales 2052, Australia*

¶*Universidade Federal do Ceará, Departamento de Física Caixa Postal 6030, 60455-760 Fortaleza, Ceará, Brazil*

§*Department of Physics, University of Antwerp, Groenenborgerlaan 171, B-2020 Antwerp, Belgium*

‖*National Institute for Materials Science, Namiki 1-1, Tsukuba, Ibaraki 305-0044, Japan*

⊥*School of Physics and Astronomy and ARC Centre of Excellence in Future Low-Energy Electronics Technologies (FLEET), Monash University, Clayton, Victoria 3800, Australia*

#*NANOlab Center of Excellence, University of Antwerp, Antwerp, Belgium*

E-mail: feixiang.xiang@unsw.edu.au; andrey@fisica.ufc.br; milorad.milosevic@uantwerpen.be; alex.hamilton@unsw.edu.au

December 6, 2023

Abstract

The highly tunable band structure of the zero-energy Landau level (zLL) of bilayer graphene makes it an ideal platform for engineering novel quantum states. However, the zero-energy Landau level at high electric fields has remained largely unexplored. Here we present magneto-transport measurements of bilayer graphene in high transverse electric fields. We observe previously undetected Landau level crossings at filling factors $\nu = -2$, 1 and 3 at high electric fields. These crossings provide constraints for theoretical models of the zero-energy Landau level, and show that the orbital, valley and spin character of the quantum Hall states at high electric fields is very different from that in low electric fields. In particular a quantum Hall state with simultaneous orbital and valley polarization at $\nu = -2$ is found at high electric fields, and we show that transitions to states with the same filling factor yet different polarization can be controlled by the gate bias.

The zero-energy Landau level (zLL) of Bernal-stacked bilayer graphene (BLG) is unconventional, with eightfold degeneracy due to its orbital N, valley ξ, and spin σ symmetries.[1,2] In the presence of magnetic and electric fields the eightfold degeneracy can be completely lifted by electronic interactions and/or single-particle perturbations, giving rise to eight different energy levels $|N, \xi, \sigma\rangle$ labelled by their orbital, valley, and spin quantum numbers, and rich families of broken-symmetry quantum Hall (QH) states.[3–13] Applying a transverse electric field (E) causes multiple transitions between Landau levels in the zLL octet, which are phase transitions between states with different orbital, valley and spin characters.[8,14–17] The rich family of QH states and electrical tunability of the phase transitions make the zero-energy Landau level of bilayer graphene an attractive platform for exploring exotic phases of matter.[18–30]

However, modelling the eigenenergies within the zLL to determine the nature and energetic ordering of the broken-symmetry QH states is a non-trivial task. This is because the problem involves not only single-particle effects but also electron-electron interactions.[1,4,5,17–19,31] The conditions under which two Landau levels cross are crucial for understanding the relative energies of these levels and can be used to probe the nature of the states.[32–37] However the

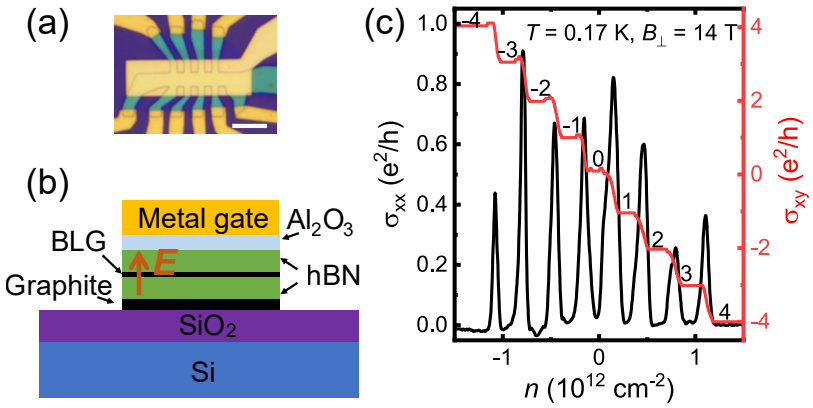

Figure 1: Device structure and characterization. (a) Optical image of the BLG device with a Hall bar structure. Scale bar: 5 μm. (b) Schematic of a cross section of the BLG device. The orange arrow gives the positive direction of electric fields E. (c) Longitudinal conductivity σ_{xx} (black) and Hall conductivity σ_{xy} (red) as a function of carrier density n at a constant electric field $E = 0.04$ V/nm for temperature $T = 170$ mK and magnetic field $B_\perp = 14$ T. The integers on the Hall plateaus indicate the filling factor of corresponding quantum Hall states.

intra-zero-energy Landau level (intra-zLL) crossings observed in BLG at low electric fields do not provide sufficient information to effectively constrain all the parameters in theoretical models of the zLL, especially parameters related to electron-electron interactions. Different theoretical models can therefore predict different orderings of the quantum numbers at the same filling factor and electric field.[15,38] To constrain the theoretical modelling more effectively requires additional information, such as the valley and orbital character of the zLL obtained from layer-resolving capacitance measurements,[17] or the orbital splitting energy determined from transport measurements.[39] Another approach to constrain the models is to examine the behaviour of the zLL at high electric fields, a regime which has remained largely unexplored.

In this work, we report magneto-transport measurements of the zero-energy Landau level of bilayer graphene over a very large range of transverse electric fields. The data show a series of new intra-zLL crossings at filling factors ν = -2, 1 and 3 at high electric fields. Unlike the intra-zLL crossings at low electric field observed previously,[15–17,22,23,38,39] the new crossings enable us to constrain the electron-electron interactions in a theoretical model

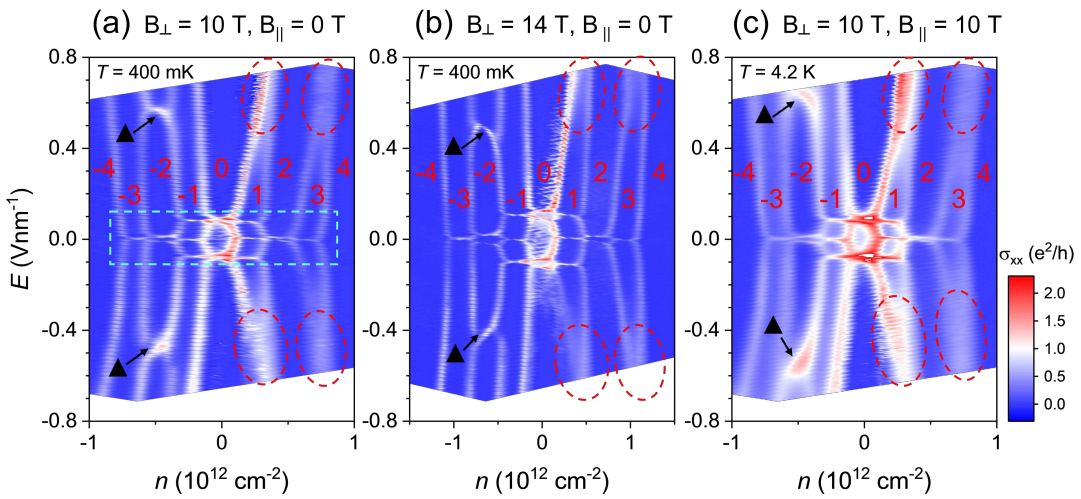

Figure 2: Intra zero-energy Landau level (intra-zLL) crossings of bilayer graphene within a wide range of electric fields. Colour maps of σ_{xx} as a function of n and E are shown for different magnetic field configurations: (a) $B_\perp$= 10 T with $B_\parallel$= 0, and (b) $B_\perp$= 14 T with $B_\parallel$= 0, both measured at T = 400 mK, and (c) $B_\perp$= 10 T with $B_\parallel$= 10 T, measured at T = 4.2 K. The white-red region and blue region indicate the maxima and minima of σ_{xx}, which represent the zLL and quantum Hall (QH) states, respectively, as described in Figure 1(c). The filling factors of each quantum Hall state are indicated. The triangles mark the sharp intra-zLL crossings at ν = -2, and red ovals the merging of two energy levels at ν = 1 and 3 at high E. The cyan rectangle emphasizes the region of low-E crossings, accessed in earlier experiments.

without relying on any other measurement techniques. We develop a minimal theoretical model that explains the energy structure and evolution of the zLL with density, magnetic and electric fields; this model is consistent with previous multi-parameter theoretical models,[17] but uses only a single fitting parameter obtained from the data. The data and model reveal that the orbital, valley, and spin character of the quantum Hall states of the zLL at high electric fields is very different from that at low electric fields, and at high electric fields we discover an electrically tunable quantum Hall state with simultaneous orbital and valley polarization at $\nu = -2$.

Figure 1(a) is an optical image of our device, with a schematic cross-section shown in Figure 1(b). The dual-gate structure allows independent control of the carrier density n and transverse electric field E. Details of the device fabrication are provided in the Supporting Information. Figure 1(c) demonstrates the high quality of the sample, showing the longitu-

dinal conductivity σ_{xx} and the Hall conductivity σ_{xy} as a function of n at $E = 0.04$ V/nm for a temperature $T = 170$ mK and a perpendicular magnetic field $B_\perp = 14$ T. The eightfold degeneracy of the zLL is fully lifted, resulting in 8 different energy levels (8 maxima in σ_{xx}) and well-resolved broken-symmetry QH states at intermediate filling factors $\nu = 0$, ±1, ±2, and ±3, identified by plateaus in σ_{xy}.

In Figure 2(a) we show a σ_{xx} colour map of the zLL as a function of carrier density n and transverse electric field E extended up to $E = \pm0.77$ V/nm for $T = 400$ mK and $B_\perp = 10$ T. In the low E regime ($|E| < 0.2$ V/nm, highlighted by the rectangle in cyan) we observe the intra-zLL crossings reported previously.[15–17,22,23,38,39] Interestingly, at higher values of E new intra-zLL crossings are observed. In contrast to the crossings at low E, the new crossings exhibit strong electron-hole asymmetry: on the hole side, the crossings are sharp at ν = -2 (marked by black triangles in Figure 2), but on the electron side the energy levels gradually cross at $\nu = 1$ and 3 (marked by red ovals in Figure 2), and do not cross at $\nu = 2$.

Using an in-situ sample rotator we measure the new crossings at different magnetic fields and field orientations as shown in Figures 2(b,c), and find the new crossings at electron and hole sides exhibit different behaviour. Figure 2(b) shows a σ_{xx} colour map at $B_\perp = 14$ T and $T = 400$ mK, where one observes that the high E crossings at ν = -2 move to lower $|E|$, while those at $\nu = 1$ and 3 move to higher $|E|$. Figure 2(c) shows a σ_{xx} colour map at $T = 4.2$ K with $B_\perp = 10$ T and an in-plane magnetic field $B_\parallel = 10$ T, where the high E crossings at ν = -2 now move to even higher $|E|$ (although the exact location of the crossings of the energy levels at $\nu = 1$ and 3 is less clear due to Landau level broadening caused by the higher measurement temperature than in Figures 2(a,b).

To determine the orbital, valley and spin character of the zLL, we first focus on understanding the order of symmetry breaking in the zLL by tracking the evolution of the Landau levels at low E with increasing magnetic field. Figures 3(a-d) are high-resolution colour maps of σ_{xx} in the low E regime of the zLL for $B_\perp$ from 2.5 to 14 T. They show gradual lifting of the eightfold degeneracy of the zLL as $B_\perp$ is increased. A schematic depiction of the

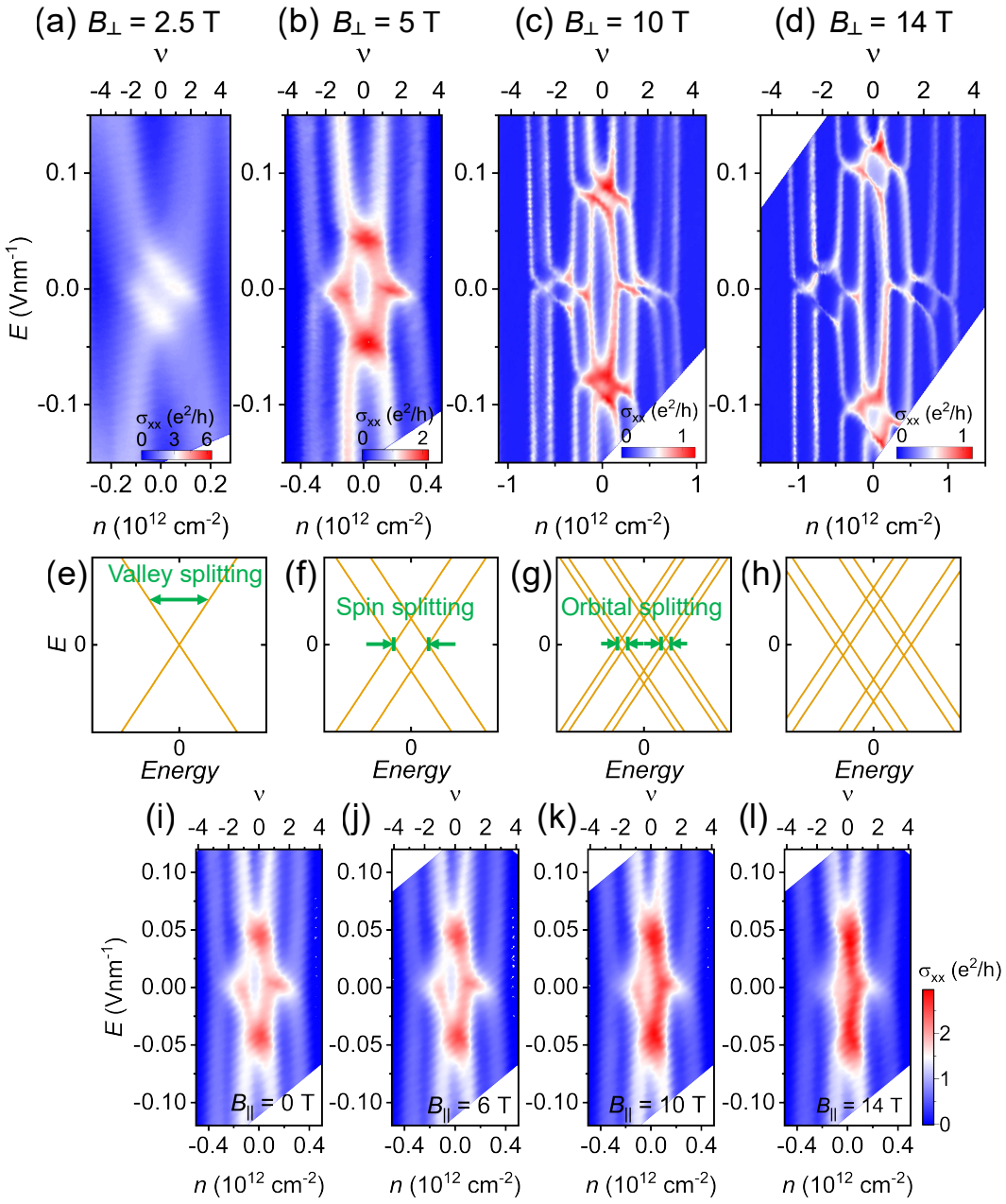

Figure 3: Evolution of broken-symmetry quantum Hall (QH) states in different magnetic fields. (a-d) Colour maps of longitudinal conductivity σ_{xx} as a function of carrier density n and transverse electric field E at T = 170 mK and $B_\perp$ = 2.5 (a), 5 (b), 10 (c) and 14 T (d). In the top x-axes, the carrier density has been converted to filling factor. (e-h) Schematics of the Landau level energies as a function of electric field for the zLL, which correspond to panels (a-d), respectively, illustrating the sequence of valley, spin, and orbital symmetry breaking with increase in $B_\perp$. The orange solid lines and white space correspond to the white/red regions and the blue region in panels (a-d), respectively. The green arrows highlight the zLL splittings at $B_\perp$ = 2.5, 5, and 10 T. (i-l) Colour plot of σ_{xx} vs n and E at T = 4.2 K, with $B_\perp$ = 5 T and $B_\parallel$ as labelled.

sequence of degeneracy lifting and evolution of the zLL energies as a function of E is shown schematically in Figs. 3(e-h). Starting at $B_\perp = 2.5$ T the zLL is nearly eightfold degenerate near $E = 0$ (Fig. 3(a)). As E increases the Landau levels split, which we associate with a lifting of the valley degeneracy (since E breaks the layer symmetry in bilayer graphene, which is equivalent to the valley symmetry in the zLL quantum Hall regime[1]).

Increasing the field to $B_\perp = 5$ T (Fig. 3(b)), the $\nu = 0$ state starts to emerge at $E = 0$ in addition to the well-resolved $\nu = 0$ state at $|E| > 0.05$ V/nm which we again associate with breaking of the valley symmetry. The emerging zLL splitting at $\nu = 0$ and $E = 0$ must therefore be associated with the breaking of either spin or orbital symmetry. To distinguish between these two possibilities we now add an in-plane component $B_\parallel$ to the perpendicular magnetic field, by tilting the sample with an *in-situ* rotator.[40] Figures 3(i-l) show colour maps of σ_{xx} in the zLL at $T = 4.2$ K and $B_\perp = 5$ T with $B_\parallel = 0$, 6, 10 and 14 T. As $B_\parallel$ increases from 0 T to 14 T there is an increase in σ_{xx} in the region near $E = 0$ and $n = 0$, indicated by the σ_{xx} colour map changing from white to red color. This increase suggests the Landau level splitting at $\nu = 0$ is getting smaller as the in-plane magnetic field increases. Since the orbital symmetry must be insensitive to $B_\parallel$, the zLL splitting at $\nu = 0$ and $E = 0$ is therefore assigned to the breaking of spin symmetry as shown in Figure 3(f). We note that the increase of σ_{xx} at $E = 0$ and $n = 0$ with increasing $B_\parallel$ is consistent with a phase transition from a canted antiferromagnetic state to a ferromagnetic state,[20,41,42] which suggests this spin symmetry breaking at $E = 0$ and $n = 0$ is enhanced by Coulomb interactions.

Finally we attribute the zLL splitting at $E = 0$ and $\nu = \pm 2$ observed at $B_\perp = 10$ T to the breaking of the remaining orbital symmetry as shown in Figure 3(g). Figure 3(h) shows further increase of $B_\perp$ to 14 T only enlarges the zLL splitting but no additional crossings are observed.

We now proceed to develop a quantitative understanding of zero Landau level eigenenergies, and their evolution with electric and magnetic fields, to determine their orbital, spin

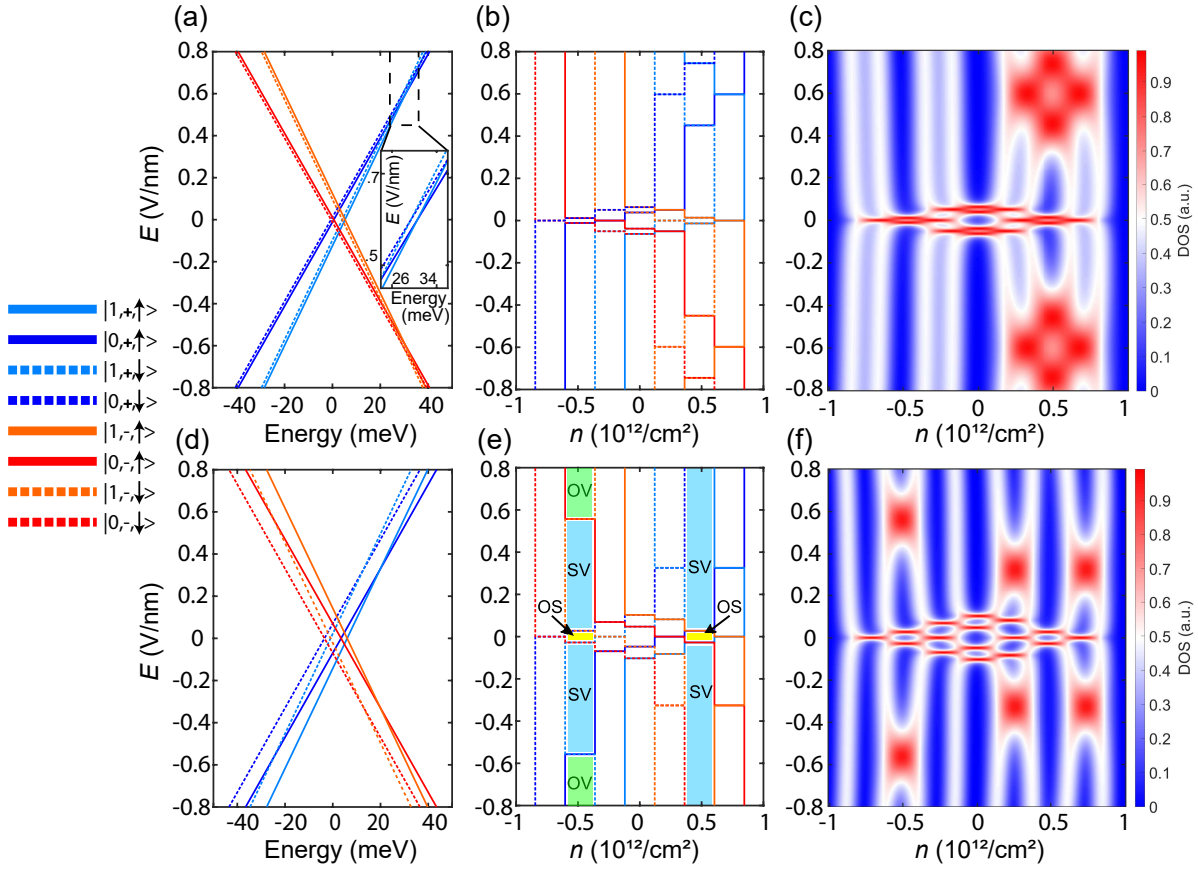

Figure 4: Theoretical models for the zero-energy Landau levels (zLL) of bilayer graphene at $B_\perp = 10$ T, which corresponds to the experimental data in Figure 2(a). Panels (a-c) show the calculation results using a single-particle model with electron-hole asymmetry terms γ_4 and Δ', and panels (d-f) the same model after including an exchange enhanced $g' = 10$ Landé factor and a Lamb shift term $\Delta_L(B_\perp)$. The legend on the left indicates the colour and line schemes used to represent different quantum states of the zLL in panels (a,b,d,e). (a,d) show the zLL energies as a function of energy and applied electric field. The inset in (a) shows a zoom-in view of the area highlighted by the dashed rectangle for better visualization of the Landau level crossings. (b,e) show the zLL energies as a function of carrier density and electric field, which are used to identify the filling sequence of the zLL at different electric fields. The color-shaded regions at $\nu = \pm 2$ show different polarized QH states. The yellow regions indicate the orbital and spin polarized states (OS), the cyan regions indicate the spin and valley polarized states (SV) and the green regions indicate the orbital and valley polarized states (OV). (c,f) show colour maps of the density of states of the zLL as a function of carrier density and electric field, calculated with a 0.5 meV energy broadening of the Landau levels.

and valley assignments. To do this we construct a theoretical model that reproduces the sequence of degeneracy liftings and level crossings observed in the experiments. We begin by showing that a single-particle model, using the well-known terms for bilayer graphene, cannot reproduce the level crossings observed experimentally – it is crucial to include the effect of interparticle interactions. However including these many body interactions is non-trivial; for example a model developed in Ref. 17 to describe the evolution of the zLL octet at low electric fields already uses 5 adjustable parameters. Therefore we build upon the parameter-free single particle model and construct a minimal theoretical model that captures the essential physics, while requiring only a single fitting parameter.

To illustrate the development of the model, we start by examining the evolution of the zLL octet at $B_\perp = 10$ T, as depicted in Figure 2(a). Previously it was shown that the *inter*-Landau level crossings in BLG at high electric field (different from the *intra*-level crossings of the zLL octet studied here) could be described using a single-particle model.[36] We adopt a similar single-particle model as our starting point. To account for the pronounced electron-hole asymmetry observed in intra-zLL crossings at high electric fields, we add electron-hole asymmetry terms γ_4 and Δ' into the model. Here, γ_4 is second nearest neighbor interlayer hopping, while Δ' is on-site energy (see Supporting Information for full details). The resulting eigenenergies of the zLL within this model are:

$$\begin{cases} E_0 = \frac{1}{2}\xi u \pm \frac{1}{2} g\mu_B B, \\ E_1 = \frac{1}{2}\xi u + \eta\left(\frac{2\gamma_4\gamma_1}{\gamma_0} + \Delta' - \xi u\right) \pm \frac{1}{2} g\mu_B B, \end{cases} \tag{1}$$

where γ_0 and γ_1 are the intralayer and interlayer nearest-neighbor hopping, $\xi = \pm 1$ accounts for the K and K′ valleys, $\eta = \hbar\omega_c/\gamma_1$ and ω_c is the cyclotron frequency, and $g = 2$ is the normal Zeeman g-factor.[2] The interlayer bias potential u is related to the electric field as $u = CE$, with the effective capacitance $C = 0.1$ eVnm/V.[36,43]

However, the results from Eq. (1), shown in Figures 4(a-c), indicate this single-particle approach is inadequate. First, although this single-particle model predicts the correct 16

crossings at $|E| < 0.2$ V/nm, it incorrectly predicts the Landau level crossings at high E. The experimental data in Figure 2(a) shows high E crossings at $\nu = -2$ on the hole side (highlighted by the black triangle), but on the electron side the crossings are at $\nu = 1$ and at $\nu = 3$ (highlighted by the red ovals). In contrast Eq. (1) predicts no intra-zLL crossings for high E on the hole side (Fig. 4(c)), while on the electron side, there are not only crossings at $\nu = 1$ and 3, but also predicted crossings at $\nu = 2$ that are not observed experimentally (Fig. 2(a)). Second, the predicted order of symmetry breaking disagrees with the one deduced from the experimental data in Figure 3. In the experiment, the $\nu = 0$ state at $E = 0$ is due to spin splitting and the $\nu = \pm 2$ states at $E = 0$ are due to orbital splitting. Instead, as shown in in Figure 4(b), this single-particle model predicts the $\nu = 0$ state at $E = 0$ is due to orbital splitting and the $\nu = \pm 2$ states at $E = 0$ are due to spin splitting.

Table 1: Parameters used in the model Eqs. (1) and (2).

γ_0 (eV)	γ_1(eV)	γ_4(eV)	Δ'(eV)	g'	u (eV)	η	Δ_L (meV)
3.0	0.400	0.150	0.020	10	0.1 E	$0.0078 B_\perp$	$\frac{-1.73\sqrt{B_\perp}}{1+4.96\sqrt{B_\perp}}$

To address the failings of the single particle model, we now examine how to incorporate many-body interactions. Numerous theoretical studies have explored the influence of electron-electron interactions on the zLL.[4,5,17–19,31] In particular Ref. 17 provides detailed calculations for Coulomb interactions in the zLL, and has successfully been used to describe the intra-zLL crossings observed at low electric fields. However this model has only been applied to low electric fields and involved Hartree-Fock calculations with 5 fitting parameters, making it hard to extend to the large electric field regime explored here. Instead we introduce a minimal theoretical model that still captures the key physics, is consistent with Ref. 17, but only needs a single adjustable parameter.

We introduce two phenomenological terms to account for many body effects into Eq. (1). First we introduce an effective g-factor, g', as the sole fitting parameter to account for the Coulomb interaction enhanced spin splitting. Second, to address orbital splitting induced by

Coulomb interactions[31] we add a magnetic field dependent Lamb shift which we take directly from Ref. 17 as $\Delta_L(B_\perp) = -1.73\sqrt{B_\perp}/(1 + 4.96/\sqrt{B_\perp})$. Including these modifications, we obtain the effective energies of the zLL as:

$$\begin{cases} E_0 = \frac{1}{2}\xi u \pm \frac{1}{2}g\mu_B B \pm \frac{1}{2}g'\mu_B B_\perp, \\ E_1 = \frac{1}{2}\xi u + \eta\left(\frac{2\gamma_4\gamma_1}{\gamma_0} + \Delta' - \xi u\right) \pm \frac{1}{2}g\mu_B B \pm \frac{1}{2}g'\mu_B B_\perp + \Delta_L(B_\perp). \end{cases} \tag{2}$$

By fitting the newly discovered intra-zLL crossings at high electric fields, the fitting parameter g' associated with electron-electron interactions in the minimal model can be effectively constrained. Setting the fitting parameter g' to 10, the modelling produce results shown in Figures 4(d-f) that capture the primary features observed in the experimental data. These include the intra-zLL crossings at both low and high electric fields, the sequence of symmetry breaking with increasing electric fields and magnetic fields, as well as the orbital and valley character of the states at low electric field consistent with Ref 17. Moreover, the magnetic field dependence of the high E crossings observed at ν = -2, 1, and 3 in Figure 2 can also be reproduced, as demonstrated in Figure S5. While the model does not exactly reproduce the precise values of E where crossings happen at $\nu = 1$, and 3, the overall agreement of the model with the experimental data confirms the substantial role played by electron-electron interactions within the zLL and the effectiveness of the simplified Coulomb interaction terms. These results underline the importance of the newly discovered intra-zLL crossings at high electric fields as an alternative approach to constrain theoretical models for the zLL in BLG.

After constraining the theoretical modelling using the newly discovered intra-zLL crossings, we can determine the character of the orbital, valley and spin quantum numbers for the QH states in the zLL. This determination is based on the LL diagram shown in Figures 4(d,e), which show that the orbital, valley and spin character of the QH states at high E differs from that at low E. The different nature of the QH states observed at high E can open up new possibilities for studying quantum phases that are different than those acces-

sible at low E.[22,23,25–28] In the following paragraphs we discuss two examples of new physics accessible at high electric fields.

A first example is the observation of new QH states at filling factor $\nu = -2$ when a large E is applied to tune the system above the new crossings. There are two types of $\nu = \pm 2$ states at high magnetic fields observed in previous works.[11,15,22] One type (OS) is near zero electric field, as highlighted by yellow shading in Figure 4(e), which is simultaneously orbital and spin polarized. The occupied zLLs in this case share the same orbital and spin quantum numbers $|1, \downarrow\rangle$ at $\nu = -2$ and $|0, \uparrow\rangle$ at $\nu = 2$. The other type of state (SV) is found at finite electric fields, as highlighted by the cyan shading Figure 4(e), which are simultaneously spin and valley polarized. The occupied zLLs share quantum numbers $|-, \uparrow\rangle$ at $\nu = -2$ and $|+, \downarrow\rangle$ at $\nu = 2$. Distinct from the latter two types of states, the $\nu = -2$ states at E above the new crossings share the same orbital and valley quantum numbers $|1, -\rangle$, which are simultaneously orbital and valley polarized and represent the third (OV) type of $\nu = -2$ QH states. We thus reveal the transition between SV and OV polarised states at $\nu = -2$ by tuning the transverse electric field, which provides a novel route to probe the spin-orbit coupling in graphene, and potentially to manipulate spins just with gate biases by rapidly driving transitions between SV and OV polarised states.

A second example is the observation of a strong asymmetry in the evolution of the electron and hole Landau levels at high E, which can be seen in the experimental data of Figure 2. Unusually the width of the blue $\nu = 1$ σ_{xx} minima at large E decreases linearly with increasing displacement field $|E|$, while the width of the σ_{xx} minima at $\nu = 0$ increases linearly, such that the σ_{xx} maximum separating $\nu = 0$ and $\nu = 1$ has a diagonal evolution across the $E - n$ plane. A similar diagonal behaviour can also been observed at $\nu = 2$ and $\nu = 3$ in the large E regime. This unexpected evolution of the σ_{xx} minima, which can only be detected because of the large range of E available experimentally, does not occur for negative filling factors such as $\nu = -1$ and $\nu = -3$, whose widths are unaffected by E. This behavior is at odds with the modelling results in Figure 4f, and cannot be explained by finite

Landau level broadening or known quantum capacitance effects (Supporting Information section II.VII). So far this observation remains unexplained: we note that in these two cases the Landau level gap is small and closes very gradually with increasing $|E|$ at $\nu = 1$ and $\nu = 3$ (see Figure 4d). Furthermore it is interesting to note that the diagonal evolution only occurs when two Landau levels with the same spin and valley, but different orbital, quantum numbers are involved: The $\nu = 0 \rightarrow 1$ transition is between $|1, +, \downarrow\rangle$ and $|0, +, \downarrow\rangle$ states, while the $\nu = 2 \rightarrow 3$ transition is between $|1, +, \uparrow\rangle$ and $|0, +, \uparrow\rangle$. This suggests that exchange effects between two levels with different orbital characters may play a role, and merits further study.

In summary, our transport measurements probed the zero-energy Landau levels of bilayer graphene over a significantly wider range of electric fields than to date. The data revealed new intra-zLL crossings at high E at filling factor -2, 1 and 3, that moreover exhibit strong electron-hole asymmetry. The observation of these novel intra-zLL crossings enabled the construction of a minimal theoretical model with only a single fitting parameter, and allowed us to obtain the character of orbital, valley and spin quantum numbers for the zLL. This in turn led to the identification of the previously unseen both spin- and valley-polarised quantum Hall states with filling factor -2 at high electric fields, and map out their transition to otherwise polarised states with same filling factor when lowering the field. The detailed Landau level spectrum of bilayer graphene presented here is not only of fundamental importance, but also provides a route towards electrically tunable strongly-correlated phases and precisely controlled transitions between diverse polarised states.

Acknowledgements We acknowledge useful discussions with Lucian Covaci, Lan Wang, and Oleg P. Sushkov, and thank one of the referees for insightful questions regarding the high field behaviour of the pleateau widths. This research was supported by the Australian Research Council Centre of Excellence in Future Low-Energy Electronics Technologies (FLEET), project No. CE170100039, funded by the Australian Government. This work was performed in part using facilities of the NSW Node of the Australian National Fabrication

Facility. AC acknowledges financial support from the Brazilian Research Council (CNPq), under the UNIVERSAL and PQ programs. AC, FMP, DN, and MVM acknowledge support by the Research Foundation - Flanders (FWO).

References

(1) McCann, E.; Fal'ko, V. I. Landau-Level Degeneracy and Quantum Hall Effect in a Graphite Bilayer. *Phys. Rev. Lett.* **2006**, *96*, 086805.

(2) McCann, E.; Koshino, M. The electronic properties of bilayer graphene. *Reports on Progress in Physics* **2013**, *76*, 056503.

(3) Ezawa, M. Intrinsic Zeeman Effect in Graphene. *Journal of the Physical Society of Japan* **2007**, *76*, 094701.

(4) Barlas, Y.; Côté, R.; Nomura, K.; MacDonald, A. H. Intra-Landau-Level Cyclotron Resonance in Bilayer Graphene. *Phys. Rev. Lett.* **2008**, *101*, 097601.

(5) Abanin, D. A.; Parameswaran, S. A.; Sondhi, S. L. Charge 2e Skyrmions in Bilayer Graphene. *Phys. Rev. Lett.* **2009**, *103*, 076802.

(6) Feldman, B. E.; Martin, J.; Yacoby, A. Broken-symmetry states and divergent resistance in suspended bilayer graphene. *Nature Physics* **2009**, *5*, 889–893.

(7) Zhao, Y.; Cadden-Zimansky, P.; Jiang, Z.; Kim, P. Symmetry Breaking in the Zero-Energy Landau Level in Bilayer Graphene. *Phys. Rev. Lett.* **2010**, *104*, 066801.

(8) Weitz, R. T.; Allen, M. T.; Feldman, B. E.; Martin, J.; Yacoby, A. Broken-Symmetry States in Doubly Gated Suspended Bilayer Graphene. *Science* **2010**, *330*, 812–816.

(9) Velasco, J.; Jing, L.; Bao, W.; Lee, Y.; Kratz, P.; Aji, V.; Bockrath, M.; Lau, C. N.; Varma, C.; Stillwell, R.; Smirnov, D.; Zhang, F.; Jung, J.; MacDonald, A. H. Trans-

port spectroscopy of symmetry-broken insulating states in bilayer graphene. *Nature Nanotechnology* **2012**, *7*, 156–160.

(10) Zhang, F.; MacDonald, A. H. Distinguishing Spontaneous Quantum Hall States in Bilayer Graphene. *Phys. Rev. Lett.* **2012**, *108*, 186804.

(11) Velasco Jr, J.; Lee, Y.; Zhang, F.; Myhro, K.; Tran, D.; Deo, M.; Smirnov, D.; MacDonald, A. H.; Lau, C. N. Competing ordered states with filling factor two in bilayer graphene. *Nature Communications* **2014**, *5*, 4550.

(12) Shi, Y.; Lee, Y.; Che, S.; Pi, Z.; Espiritu, T.; Stepanov, P.; Smirnov, D.; Lau, C. N.; Zhang, F. Energy Gaps and Layer Polarization of Integer and Fractional Quantum Hall States in Bilayer Graphene. *Phys. Rev. Lett.* **2016**, *116*, 056601.

(13) Li, J.; Fu, H.; Yin, Z.; Watanabe, K.; Taniguchi, T.; Zhu, J. Metallic Phase and Temperature Dependence of the $\nu = 0$ Quantum Hall State in Bilayer Graphene. *Phys. Rev. Lett.* **2019**, *122*, 097701.

(14) Kim, S.; Lee, K.; Tutuc, E. Spin-Polarized to Valley-Polarized Transition in Graphene Bilayers at $\nu = 0$ in High Magnetic Fields. *Phys. Rev. Lett.* **2011**, *107*, 016803.

(15) Lee, K.; Fallahazad, B.; Xue, J.; Dillen, D. C.; Kim, K.; Taniguchi, T.; Watanabe, K.; Tutuc, E. Chemical potential and quantum Hall ferromagnetism in bilayer graphene. *Science* **2014**, *345*, 58–61.

(16) Maher, P.; Wang, L.; Gao, Y.; Forsythe, C.; Taniguchi, T.; Watanabe, K.; Abanin, D.; Papić, Z.; Cadden-Zimansky, P.; Hone, J.; Kim, P.; Dean, C. R. Tunable fractional quantum Hall phases in bilayer graphene. *Science* **2014**, *345*, 61–64.

(17) Hunt, B. M.; Li, J. I. A.; Zibrov, A. A.; Wang, L.; Taniguchi, T.; Watanabe, K.; Hone, J.; Dean, C. R.; Zaletel, M.; Ashoori, R. C.; Young, A. F. Direct measurement

of discrete valley and orbital quantum numbers in bilayer graphene. *Nature Communications* **2017**, *8*, 948.

(18) Apalkov, V. M.; Chakraborty, T. Stable Pfaffian State in Bilayer Graphene. *Phys. Rev. Lett.* **2011**, *107*, 186803.

(19) Papić, Z.; Abanin, D. A. Topological Phases in the Zeroth Landau Level of Bilayer Graphene. *Phys. Rev. Lett.* **2014**, *112*, 046602.

(20) Maher, P.; Dean, C. R.; Young, A. F.; Taniguchi, T.; Watanabe, K.; Shepard, K. L.; Hone, J.; Kim, P. Evidence for a spin phase transition at charge neutrality in bilayer graphene. *Nature Physics* **2013**, *9*, 154–158.

(21) Ki, D.-K.; Fal'ko, V. I.; Abanin, D. A.; Morpurgo, A. F. Observation of Even Denominator Fractional Quantum Hall Effect in Suspended Bilayer Graphene. *Nano Letters* **2014**, *14*, 2135–2139.

(22) Zibrov, A. A.; Kometter, C.; Zhou, H.; Spanton, E. M.; Taniguchi, T.; Watanabe, K.; Zaletel, M. P.; Young, A. F. Tunable interacting composite fermion phases in a half-filled bilayer-graphene Landau level. *Nature* **2017**, *549*, 360–364.

(23) Li, J. I. A.; Tan, C.; Chen, S.; Zeng, Y.; Taniguchi, T.; Watanabe, K.; Hone, J.; Dean, C. R. Even-denominator fractional quantum Hall states in bilayer graphene. *Science* **2017**, *358*, 648–652.

(24) Perali, A.; Neilson, D.; Hamilton, A. R. High-Temperature Superfluidity in Double-Bilayer Graphene. *Phys. Rev. Lett.* **2013**, *110*, 146803.

(25) Liu, X.; Watanabe, K.; Taniguchi, T.; Halperin, B. I.; Kim, P. Quantum Hall drag of exciton condensate in graphene. *Nature Physics* **2017**, *13*, 746–750.

(26) Li, J. I. A.; Taniguchi, T.; Watanabe, K.; Hone, J.; Dean, C. R. Excitonic superfluid phase in double bilayer graphene. *Nature Physics* **2017**, *13*, 751–755.

(27) Liu, X.; Li, J. I. A.; Watanabe, K.; Taniguchi, T.; Hone, J.; Halperin, B. I.; Kim, P.; Dean, C. R. Crossover between strongly coupled and weakly coupled exciton superfluids. *Science* **2022**, *375*, 205–209.

(28) Huang, K.; Fu, H.; Hickey, D. R.; Alem, N.; Lin, X.; Watanabe, K.; Taniguchi, T.; Zhu, J. Valley Isospin Controlled Fractional Quantum Hall States in Bilayer Graphene. *Phys. Rev. X* **2022**, *12*, 031019.

(29) Zhao, T.; Balram, A. C.; Jain, J. K. Composite Fermion Pairing Induced by Landau Level Mixing. *Phys. Rev. Lett.* **2023**, *130*, 186302.

(30) Yazdani, A.; von Oppen, F.; Halperin, B. I.; Yacoby, A. Hunting for Majoranas. *Science* **2023**, *380*, eade0850.

(31) Shizuya, K. Structure and the Lamb-shift-like quantum splitting of the pseudo-zero-mode Landau levels in bilayer graphene. *Phys. Rev. B* **2012**, *86*, 045431.

(32) Poortere, E. P. D.; Tutuc, E.; Papadakis, S. J.; Shayegan, M. Resistance Spikes at Transitions Between Quantum Hall Ferromagnets. *Science* **2000**, *290*, 1546–1549.

(33) Zhu, J.; Stormer, H. L.; Pfeiffer, L. N.; Baldwin, K. W.; West, K. W. Spin Susceptibility of an Ultra-Low-Density Two-Dimensional Electron System. *Phys. Rev. Lett.* **2003**, *90*, 056805.

(34) Taychatanapat, T.; Watanabe, K.; Taniguchi, T.; Jarillo-Herrero, P. Quantum Hall effect and Landau-level crossing of Dirac fermions in trilayer graphene. *Nature Physics* **2011**, *7*, 621–625.

(35) Varlet, A.; Bischoff, D.; Simonet, P.; Watanabe, K.; Taniguchi, T.; Ihn, T.; Ensslin, K.; Mucha-Kruczyński, M.; Fal'ko, V. I. Anomalous Sequence of Quantum Hall Liquids Revealing a Tunable Lifshitz Transition in Bilayer Graphene. *Phys. Rev. Lett.* **2014**, *113*, 116602.

(36) Pan, C.; Wu, Y.; Cheng, B.; Che, S.; Taniguchi, T.; Watanabe, K.; Lau, C. N.; Bockrath, M. Layer Polarizability and Easy-Axis Quantum Hall Ferromagnetism in Bilayer Graphene. *Nano Letters* **2017**, *17*, 3416–3420.

(37) Das, I.; Lu, X.; Herzog-Arbeitman, J.; Song, Z.-D.; Watanabe, K.; Taniguchi, T.; Bernevig, B. A.; Efetov, D. K. Symmetry-broken Chern insulators and Rashba-like Landau-level crossings in magic-angle bilayer graphene. *Nature Physics* **2021**, *17*, 710–714.

(38) Kou, A.; Feldman, B. E.; Levin, A. J.; Halperin, B. I.; Watanabe, K.; Taniguchi, T.; Yacoby, A. Electron-hole asymmetric integer and fractional quantum Hall effect in bilayer graphene. *Science* **2014**, *345*, 55–57.

(39) Li, J.; Tupikov, Y.; Watanabe, K.; Taniguchi, T.; Zhu, J. Effective Landau Level Diagram of Bilayer Graphene. *Phys. Rev. Lett.* **2018**, *120*, 047701.

(40) Yeoh, L. A.; Srinivasan, A.; Martin, T. P.; Klochan, O.; Micolich, A. P.; Hamilton, A. R. Piezoelectric rotator for studying quantum effects in semiconductor nanostructures at high magnetic fields and low temperatures. *Review of Scientific Instruments* **2010**, *81*, 113905.

(41) Kharitonov, M. Canted Antiferromagnetic Phase of the ν=0 Quantum Hall State in Bilayer Graphene. *Phys. Rev. Lett.* **2012**, *109*, 046803.

(42) Pezzini, S.; Cobaleda, C.; Piot, B. A.; Bellani, V.; Diez, E. Critical point for the canted antiferromagnetic to ferromagnetic phase transition at charge neutrality in bilayer graphene. *Phys. Rev. B* **2014**, *90*, 121404.

(43) Zhang, Y.; Tang, T.-T.; Girit, C.; Hao, Z.; Martin, M. C.; Zettl, A.; Crommie, M. F.; Shen, Y. R.; Wang, F. Direct observation of a widely tunable bandgap in bilayer graphene. *Nature* **2009**, *459*, 820–823.

Supporting Information: Intra zero-energy Landau level crossings in bilayer graphene at high electric field

Feixiang Xiang,[*,†,‡] Abhay Gupta,[†,‡] Andrey Chaves,[*,¶,§] Zeb E. Krix,[†,‡] Kenji Watanabe,[‖] Takashi Taniguchi,[‖] Michael S. Fuhrer,[⊥] François M. Peeters,[§,¶] David Neilson,[§,‡] Milorad V. Milošević,[*,§,#] and Alexander R. Hamilton[*,†,‡]

†*School of Physics, University of New South Wales, Sydney, New South Wales 2052, Australia*

‡*ARC Centre of Excellence in Future Low-Energy Electronics Technologies, University of New South Wales, Sydney, New South Wales 2052, Australia*

¶*Universidade Federal do Ceará, Departamento de Física Caixa Postal 6030, 60455-760 Fortaleza, Ceará, Brazil*

§*Department of Physics, University of Antwerp, Groenenborgerlaan 171, B-2020 Antwerp, Belgium*

‖*National Institute for Materials Science, Namiki 1-1, Tsukuba, Ibaraki 305-0044, Japan*

⊥*School of Physics and Astronomy and ARC Centre of Excellence in Future Low-Energy Electronics Technologies (FLEET), Monash University, Clayton, Victoria 3800, Australia*

#*NANOlab Center of Excellence, University of Antwerp, Antwerp, Belgium*

E-mail: feixiang.xiang@unsw.edu.au; andrey@fisica.ufc.br; milorad.milosevic@uantwerpen.be; alex.hamilton@unsw.edu.au

Section I: Experimental methods

I.I. Device fabrication

The bilayer graphene (BLG) van der Waals (vdW) heterostructure was fabricated by the dry transfer method.[1,2] Flakes of BLG, hexagon boron nitride (hBN) and graphite were exfoliated onto the Si/SiO_2 substrates using the mechanical exfoliation method. To reduce the polymer residues, cleanroom blue tapes were used to exfoliate the 2D material flakes. The blue tapes with the 2D material flakes were pressed on clean Si/SiO_2 substrates, which were then heated on a hotplate at 110^oC for 2 minutes before peeling off the blue tapes in order to increase the size of BLG flakes.[3] The Si/SiO_2 substrates used for exfoliating BLG and graphite were also treated by oxygen plasma for 5 minutes to obtain large size flakes. Optical microscope and atomic force microscope were used to find area free from polymer residues and defects in the flakes.

A polycarbonate (PC) film/polydimethylsiloxane (PDMS) stamp mounted on a glass slide was used to pick up top hBN, BLG, bottom hBN and graphite flake in sequence at temperature between 90 ^oC to 100 ^oC. The final vdW heterostructure with PC film was released on to a clean Si/SiO_2 substrate at 180 ^oC, which was followed by a rinse in chloroform for 10 mins to remove the PC film.

E-beam lithography and reactive ion etching (40 sccm CHF_3 and 4 sccm O_2) were used to shape the BLG vdW heterostructure into a Hall bar device structure. Cr/Au were deposited on exposed edges of BLG and bottom graphite gate electrode using thermal evaporation to make electrical contacts. A 15 nm Al_2O_3 was deposited by atomic layer deposition and then a top Ti/Au gate electrode was defined by e-beam lithography and thermal evaporation.

I.II. Electrical transport measurements

Electrical transport measurements were performed using lock-in techniques with excitation frequency 77 Hz and 10 to 100 nA current in a dilution fridge with an in-situ 2 axis piezo-

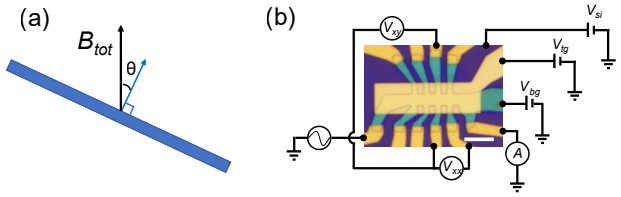

Figure S 1: (a) Alignment of magnetic field B relative to layers. (b) Schematics of the electrical transport measurement setup.

electric rotator, and a 15 T superconducting magnet. The temperature was set between 170 mK and 4.2 K, which correspond to the cold finger temperatures and were measured using a RuOx thermometer. Unless specified, the magnetic field is perpendicular to the basal plane of BLG. When there is a parallel field component, the sample is tilted relative to the total magnetic field direction in an angle θ as shown in Fig. S1a. The magnetic field and the tilted angle θ for the tilted field measurements are shown in the Table S1.

Table 1: Magnetic fields and tilt angles in the tilted field measurements.

$B_\perp$ (T)	$B_\parallel$ (T)	B_{tot} (T)	θ (^{o})
5	0	5.00	0.00
5	6	7.81	50.19
5	10	11.18	63.43
5	14	14.87	70.35
10	10	14.14	45.00

Figure S1b shows a schematic of the measurement circuit for the BLG sample. Longitudinal resistivity ρ_{xx} and Hall resistivity ρ_{xy} were recorded while varying magnetic fields, top and bottom gate voltages. A voltage was applied to the doped Si substrate to minimize the contact resistance between metal electrodes and BLG sample. Longitudinal conductivity $\sigma_{xx} = \rho_{xx}/(\rho_{xx}^2 + \rho_{xy}^2)$ and Hall conductivity $\sigma_{xy} = \rho_{xy}/(\rho_{xx}^2 + \rho_{xy}^2)$ are retrieved from the resistivity data.

Figure S2 shows the longitudinal resistivity ρ_{xx} as a function of top and bottom gate voltages at $B = 0$ T and $T = 4.2$ K, where we find the charge neutrality point to be located at $V_{tg,0} = -0.85$ V and $V_{bg,0} = 0.11$ V. The bottom graphite gate and top metal gate are

used to independently tune n and transverse electric field E across the sample,

$$n = C_{bg}(V_{bg} - V_{bg,0})/e + C_{tg}(V_{tg} - V_{tg,0})/e, \tag{1}$$

$$E = \frac{1}{2\epsilon_0}[C_{bg}(V_{bg} - V_{bg,0}) - C_{tg}(V_{tg} - V_{tg,0})] \tag{2}$$

The capacitance per unit area of bottom and top gates calculated from LL spectrum are 74.9 nF/cm^2 and 150.5 nF/cm^2, respectively.

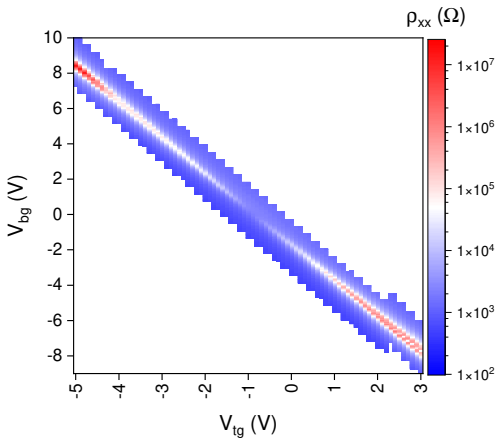

Figure S 2: Longitudinal resistivity ρ_{xx} as a function of top and bottom gate voltages at $T = 4.2$ K and zero magnetic field.

Section II: Theoretical Modelling of the zero-energy Landau level

II.I. Single-particle Hamiltonian

Bilayer graphene (BLG) has four atoms in the unit cells, two in each layer, which can be denoted here by (A1,B1) and (A2,B2) respectively in AB-stacked configuration.[4–6] A and B represents the two sublattices of the honeycomb crystal structure, whereas numbers 1 and 2 represent the two layers. In the tight-binding approach, we define different hopping parameters between different atomic sites: γ_0 is the hopping between adjacent atomic sites

in each layer i.e. A1 and B1 or A2 and B2; γ_1 is the inter-layer hopping between dimer sites A2 and B1; γ_3 is the inter-layer hopping between non-dimer sites A1 and B2; and γ_4 is the inter-layer hopping between a dimer and a non-dimer site, A1 and A2 or B1 and B2.

In the vicinity of K points of the Brillouin zone, one can write the 4×4 Hamiltonian for BLG in the basis (A1,B1,A2,B2),[4]

$$H = \begin{bmatrix} \epsilon_{A1} & v\pi^\dagger & -v_4\pi^\dagger & v_3\pi \\ v\pi & \epsilon_{B1} & \gamma_1 & -v_4\pi^\dagger \\ -v_4\pi & \gamma_1 & \epsilon_{A2} & v\pi^\dagger \\ v_3\pi^\dagger & -v_4\pi & v\pi & \epsilon_{B2} \end{bmatrix}, \tag{3}$$

where, $\pi^\dagger = p_x - ip_y$, $\pi = p_x + ip_y$, individual velocities can be related to the hopping energies as $v = \sqrt{3}a\gamma_0/2\hbar$, $v_3 = \sqrt{3}a\gamma_3/2\hbar$, $v_4 = \sqrt{3}a\gamma_4/2\hbar$, and $a = 0.246$nm is the lattice constant. The Hamiltonian for electrons around the K' points are obtained by replacing $\pi^\dagger \leftrightarrow \pi$, A1$\leftrightarrow$B2, B1$\leftrightarrow$A2, and by changing the sign of the inter-layer bias potential, if any.

In the presence of inter-layer bias, we define $\epsilon_{A1} = -u/2$, $\epsilon_{B1} = -u/2+\Delta'$, $\epsilon_{A2} = u/2+\Delta'$, and $\epsilon_{B2} = u/2$, where, u is the inter-layer potential difference and Δ' is the energy difference between the dimer and non-dimer sites. In the presence of magnetic field of the order of a few Tesla, the effect of γ_3 on Landau levels is not noticeable for $\gamma_3/\gamma_0 \leq 0.2$,[7] which is generally the case (see e.g. Table 1 of Ref. 4). Hence, we neglect the effect of γ_3, and the resulting 4×4 Hamiltonian reads

$$H = \begin{bmatrix} -u/2 & 0 & -v_4\pi^\dagger & v\pi^\dagger \\ 0 & u/2 & v\pi & -v_4\pi \\ -v_4\pi & v\pi^\dagger & u/2+\Delta' & \gamma_1 \\ v\pi & -v_4\pi^\dagger & \gamma_1 & -u/2+\Delta' \end{bmatrix}, \tag{4}$$

where the basis has been rearranged as (A1,B2,A2,B1), for convenience.

II.II. Low-energy 2×2 Hamiltonian

The 4 × 4 Hamiltonian can be broken into separate 2× 2 blocks, in order to obtain a Hamiltonian that captures only the low-energy bands of BLG. After some cumbersome algebra, considering only terms up to second order in momentum, we obtain

$$H = \begin{pmatrix} -u/2 + [uv^2/\gamma_1^2 + 2v_4v/\gamma_1 + v^2\Delta'/\gamma_1^2]\pi^\dagger\pi & -(v^2/\gamma_1)(\pi^\dagger)^2 \\ -(v^2/\gamma_1)(\pi)^2 & u/2 + [-uv^2/\gamma_1^2 + 2v_4v/\gamma_1 + v^2\Delta'/\gamma_1^2]\pi\pi^\dagger \end{pmatrix} \tag{5}$$

where,

$$\begin{aligned} h_0 &= \frac{-v^2}{\gamma_1}\begin{pmatrix} 0 & (\pi^\dagger)^2 \\ (\pi)^2 & 0 \end{pmatrix}\ ,\ h_u = \frac{-u}{2}\left[\begin{pmatrix} 1 & 0 \\ 0 & -1 \end{pmatrix} - \tfrac{2v^2}{\gamma_1^2}\begin{pmatrix} \pi^\dagger\pi & 0 \\ 0 & -\pi\pi^\dagger \end{pmatrix}\right] \\ h_4 &= \frac{2v_4v}{\gamma_1}\begin{pmatrix} \pi^\dagger\pi & 0 \\ 0 & \pi\pi^\dagger \end{pmatrix}\ ,\ h_{\Delta'} = \frac{v^2\Delta'}{\gamma_1^2}\begin{pmatrix} \pi^\dagger\pi & 0 \\ 0 & \pi\pi^\dagger \end{pmatrix} \end{aligned} \tag{6}$$

In this Hamiltonian, the only term which changes sign from K to K' valley or from one layer to the other is h_u. In order to take this sign change into account, we introduce the parameter ξ, which can be 1 or -1 depending on the valley, so that

$$h_u = \frac{\xi u}{2}\left[\begin{pmatrix} 1 & 0 \\ 0 & -1 \end{pmatrix} - \tfrac{2v^2}{\gamma_1^2}\begin{pmatrix} \pi^\dagger\pi & 0 \\ 0 & -\pi\pi^\dagger \end{pmatrix}\right] \tag{7}$$

In the presence of magnetic field, a vector potential is introduced to the Hamiltonian,

which changes the $\mathbf{p} \rightarrow (\mathbf{p} - e\mathbf{A})$. Using Landau gauge $\mathbf{A} = (0, Bx, 0)$, p_y changes to $p_y - eBx$. As a result, $\pi^\dagger$ and π act as raising and lowering operators, respectively, such that:[4]

$$\pi^\dagger \, \phi_l = i\sqrt{2\hbar eB(l+1)} \, \phi_{l+1} \quad , \quad \pi \, \phi_l = -i\sqrt{2\hbar eB(l)} \, \phi_{l-1} \tag{8}$$

We define the basis as $|0\rangle = (\phi_0, 0)$, $|1\rangle = (\phi_1, 0)$; $|2l-2\rangle = (0, \phi_{l-2})$, $|2l-1\rangle = (\phi_l, 0)$; $\forall \;\; l \geq 2$, similar to Ref. 8.

As we are only interested in the LL octet, we just need the eigenvalues for $l = 0, 1$. For $l = 0$, only the first term of h_u is non-zero, which yields $E_0 = \xi u/2$. For $l = 1$, all terms in Eq. (6), except for h_0, contribute to give $E_1 = \xi u/2 + (-\xi u + 2\gamma_4\gamma_1/\gamma_0 + \Delta')\eta$, where $\eta = \hbar\omega_c/\gamma_1$ and ω_c is the cyclotron frequency.

II.III. Lamb-shift-like correction

The orbital degeneracy of the zero-energy LL is expected to be lifted by Coulomb quantum fluctuations of the Dirac sea (valence band) due to the different spatial distributions of $l = 0$ and $l = 1$ orbitals.[9] This effect bears resemblance with the Lamb-shift[10] that lifts the degeneracy of two states in the Hydrogen atom.

In our model, we define a Lamb-shift-like term of the form fE_C, where f is a pre-factor that controls the strength of the Coulomb interaction, $E_C = \frac{e^2}{4\pi\epsilon^{||}_{BN}}\sqrt{\frac{eB}{\hbar}}$ is the Coulomb screening due to the hBN layer, for which the dielectric constant is taken as $\epsilon^{||}_{BN} = 6.6\epsilon_0$.[6] We point out that the magnetic length used in this calculation depends only on the magnetic field component perpendicular to the BLG layers. The pre-factor f is then taken to be $-\frac{0.2}{1+2.73a_{scr}}$, where $a_{scr} \approx \frac{0.67E_C}{\hbar\omega_c}$, as considered in previous calculations.[6] The Coulomb exchange per electron while completely filling $l = 1$ orbital is greater than that for $l = 0$ orbital under particle-hole symmetry approximation,[9] hence, the Lamb-shift correction can be added to

just one of these orbitals with appropriate signs. We thus obtain

$$\begin{aligned} E_0 &= \frac{1}{2}\xi u \pm \frac{1}{2} g\mu_B \sqrt{B_\perp^2 + B_{||}^2}, \\ E_1 &= \frac{1}{2}\xi u - \xi\eta u \pm \frac{1}{2} g\mu_B \sqrt{B_\perp^2 + B_{||}^2} + (2\gamma_4\gamma_1/\gamma_0 + \Delta')\eta - \frac{1.73\sqrt{B_\perp}}{1 + 4.96\sqrt{B_\perp}}, \end{aligned} \tag{9}$$

where we now also account for the possibility of having a tilted magnetic field, with out-of-plane and in-plane components defined as $B_\perp$ and $B_{||}$, respectively. Notice we have also added Zeeman spin splitting terms to the eigenenergies, where $g \approx 2$ is the Landé g-factor and μ_B is the Bohr magneton.

II.IV. Exchange-enhanced spin splitting

There is evidence of strong electron correlations leading to the breaking of spin symmetry near the charge neutrality point in BLG, which increases monotonically with perpendicular magnetic field.[11,12] To account for this, we modify the Zeeman spin splitting term assuming an effective Landé factor g'. Notice this term depends only on the magnetic field component perpendicular to the BLG. In fact, similar kind of term has been previously added heuristically to understand the BLG system.[5]

Hence, the final expression for the lowest LL energy spectrum, given as Eq. (2) of the main text, reads

$$\begin{aligned} E_0 &= \frac{1}{2}\xi u \pm \frac{1}{2} g\mu_B \sqrt{B_\perp^2 + B_{||}^2} \pm \frac{1}{2} g'\mu_B B_\perp, \\ E_1 &= \frac{1}{2}\xi u - \xi\eta u \pm \frac{1}{2} g\mu_B \sqrt{B_\perp^2 + B_{||}^2} + (2\gamma_4\gamma_1/\gamma_0 + \Delta')\eta - \frac{1.73\sqrt{B_\perp}}{1 + 4.96\sqrt{B_\perp}} \pm \frac{1}{2} g'\mu_B B_\perp. \end{aligned} \tag{10}$$

II.V. Model Parameters

From Raman and infrared spectroscopy, different hopping energies for bilayer graphene have been obtained in previous works: for instance, from Ref. 13, the effective mass around the K and K' points in BLG is observed to be in the range of $0.03 - 0.07 m_e$. γ_0 and the effective

mass m are related by $\gamma_0 = \sqrt{\frac{2\gamma_1}{3m}}\frac{\hbar}{a}$. We thus assume mass $m = 0.037m_e$, which yields $\gamma_0 = 3$ eV,[4] as stated in the main manuscript.

The factor C converting potential energy to electric fields $u = CE$ has been observed to be between 100-200 meVnm/V.[8,14] We have assumed it to be 100 meVnm/V in our calculations, as given in Table I of the main manuscript.

To properly account for the zLL crossings observed experimentally at high $|E|$, we included the exchange enhanced Landé factor g' and the Lamb-shift-like term as we shown in the eq. (2) of the main text. We played with these two parameters in order to fine tune the theoretically obtained crossings, towards better comparison with the experimental observations.

When taking the exchange enhanced Landé factor g' added to the $l = 0, 1$ LLs as 10, and the Lamb-shift like term to be $\Delta_L = -1.73\sqrt{B_\perp}/(1+4.96/\sqrt{B_\perp})$ in accordance with previous calculations,[6] we obtained a LL spectrum that qualitatively matches the experimentally observed LL crossings as shown in Fig. 4 of the main text. Namely, it produces a strongly electron-hole asymmetric LL spectrum, which exhibits four high-$|E|$ crossings (one for each sign of electric field, at filling factors $\nu = 1$ and 3) at the positive charge density, and only two high-$|E|$ crossings (one for each sign of electric field at filling factor ν = -2) in the negative charge density part of the Figure.

Figure S3 shows examples how the g' and the Lamb-shift-like term affect the intra-zLL crossings. Figs. S3(a) and S3(b) shows the color maps of density of states as a function of carrier density n and transverse electric field E for two different g' at $B_\perp = 10$T. If we decrease g' from 10 to 8, the $\nu = -2$ high $|E|$ crossing decreases in $|E|$, as depicted in Fig S3(a), bringing the $\nu = -2$ and $\nu = 1$,3 high $|E|$ crossings closer. In the case of larger g' in Fig. S3(b), the $|E|$ values for zLL crossings for $\nu = -1, 0, 1$ at lower electric field are enhanced, whereas it is unchanged for $\nu = -2$ and 2 at lower $|E|$, which is more aligned with the low $|E|$ crossings observed experimentally. So, one can seek for the optimum exchange enhanced value to get closer to both the lower and higher $|E|$ crossings values compared to

the experiments.

The Lamb-shift like term, though derived from previous calculations,[6] can also affect the values of crossings: lower Δ_L reduces the $|E|$ values for the $\nu = -2$ high $|E|$ crossings as shown in Figs. S3(c), while increasing the values for $\nu = 1$ and 3, which makes them closer to the experimentally observed $\nu = 1$ and 3 higher $|E|$ crossings as shown in S3(d) . In addition, as we increase Δ_L, the $\nu = -2$ and 2 low $|E|$ crossings are suppressed and all the low $|E|$ crossings get closer to the experimental values, but the high $|E|$ crossings are affected negatively.

This allows us to conclude that the additional terms due to Coulomb interactions in our model for the zLL *qualitatively* predicts very well the experimental picture, which indicates that the effective Landé factor is exchange enhanced and that the Lamb-shift-like term is significant in BLG. However, an exact prediction of the actual values for g' and Δ_L, towards quantitative agreement with the experimental observations, is quite challenging and calls for more sophisticated models.

II.VI. Model plots

In the Figure 4 of main text, we have introduced model plots of the zLL as a function of energy and transverse electric field E and the zLL as a function of carrier density n and transverse electric field E, and color maps for the density of states (DOS) as a function of carrier density n and transverse electric field E. The plots of the zLL as a function of energy and E in Fig. 4(a,d) are directly from the zLL energy equations (1) and (2) in our calculations. For the plots of the zLL as a function of n and E in Fig. 4(b,e), we assume that each Landau level occupies maximum carrier density of NB/ϕ_0, where $\phi_0 = h/e$ is the magnetic flux quanta, and N is the degeneracy factor.[4]

To obtain the color maps in Fig. 4(c,f), we use a model from Ref. 15 by introducing the broadening of the zLL due to disorder. For this, we used a Lorentzian function to account for the broadening of zLL,[16] so the density of states is $DOS(E) = \frac{e}{h}B\sum_{n=1}^{8}\frac{1}{\pi}\frac{\gamma}{(E-E_n)^2+\gamma^2}$.

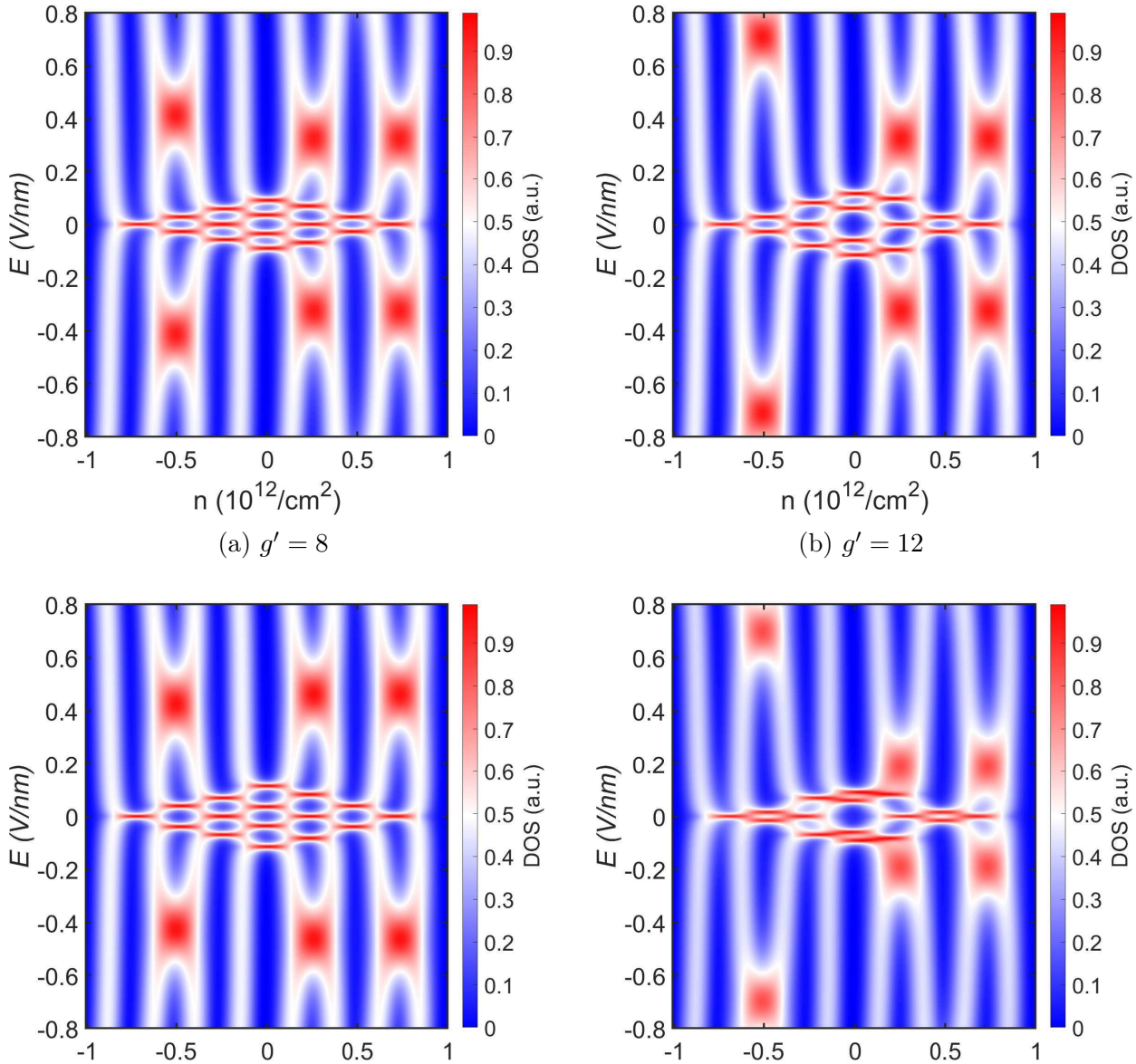

(a) $g' = 8$ (b) $g' = 12$

(c) $\Delta_L = -0.865\sqrt{B_\perp}/(1 + 4.96/\sqrt{B_\perp})$ (d) $\Delta_L = -2.595\sqrt{B_\perp}/(1 + 4.96/\sqrt{B_\perp})$

Figure S 3: Colour maps of density of states of the zLL as a function of carrier density and applied electric field field for different Coulomb interactions based model parameters. The model plots for $B_\perp = 10$T, $B_{||} = 0$T include exchange enhanced $g' = 10$ Landé factor and a Lamb shift term $\Delta_L(B_\perp)$ as described in the main text unless specified.The broadening width γ used for these plots is 0.5 meV similar to Figure 4(c) and (f) of the main text.

Here, we only calculate the density of states in the 8-fold degenerate zLL region and the broadening width γ of 0.5 meV is found to be appropriate for these plots. To highlight the effect of different disorder strengths, we plot these color maps for different broadening widths, which is discussed in the subsequent section. Next, we calculate the carrier density [$n(E_F) = \int_0^{E_F} DOS(E)\, dE$], by numerically integrating the previously obtained density of states. Finally, we plot the colormap for the density of states as a function of applied electric field and the carrier density obtained from the previous step. These plots are normalized for the density of states, therefore, DOS are given in arbitrary units (a.u.). These plots capture the main features of the experimentally observed conductivity maps: wherever the LL cross, the density of states increases, which corresponds to regions of increased conductance in the transport measurements.[15]

II.VII. Landau level broadening and quantum capacitance effect on the width (in density) of quantum Hall states

In our experimental data, measured over large range of transverse electric fields (see Fig. 2), the width (in density)of the quantum Hall states at $\nu = 0$ and 2 increases as the transverse electric field increases, but that of the states at $\nu = 1$ and 3 decrease. Meanwhile, a prominent slope in the σ_{xx} maxima between quantum Hall states at $\nu = 0$ and 1, as well as between the states at $\nu = 2$ and 3, is observed. These features are not observed on the hole side.

As an attempt to explain this observation, we first considered Landau level broadening. When the intra-zLLs cross, the density of states in the merged intra-zLL doubles. As a result, the position of σ_{xx} maximum corresponding to the intra-zLL shifts to different carrier densities. When Landau level broadening is smaller than the intra-zLL gaps near the crossings, as is the case for ν = -2, the transitions are sharp. However, when Landau level broadening is comparable to the intra-zLL gaps over relatively large range of electric fields, the transitions are expected to show a sloped lines as for the case of $\nu = 1$ and 3.

We performed theoretical modelling with different Landau level broadening using pa-

rameter γ in our model. Figure S4 show the results with γ ranging from 0.2 to 0.8 meV in steps of 0.15 meV. As Landau level broadening increase, there's a slight change in the slope of density of state (DOS) maxima and gaps as a function of transverse electric field near the crossings. However, the DOS maxima corresponding to the σ_{xx} maxima between the quantum Hall states at $\nu = 0$ and 1, and between the states at $\nu = 2$ and 3 remain predominantly vertical. Meanwhile, the width of the quantum Hall states at $\nu = 0$ and 2 remain unchanged as the transverse electric field increases.

We also considered the quantum capacitance effect, but were still unable to reproduce the experimental observation. The total capacitance is given by the equation: $1/C_{total} = 1/C_G + 1/C_Q$, where C_G represents the geometric capacitance and C_Q represents the quantum capacitance. C_Q is usually much larger than C_G, thus $1/C_{total} \approx 1/C_G$. In the gap between Landau levels, C_Q can be comparable to C_G, which decreases C_{total}.[17] Consequently, filling a Landau level would require a larger gate voltage, potentially leading to an increase the width (in density) of the quantum Hall states. The Landau level diagram in Figure 4e illustrate that the zLL exhibits a large gap at $\nu = 0$, which grows as the transverse electric field increases. This gap at $\nu = 0$ could increase the width of the corresponding quantum Hall states in our measurements, and cause the sloped σ_{xx} maximum between quantum Hall states at $\nu = 0$ and 1. However, if the large gap at $\nu = 0$ were the sole cause, then we would expect the subsequent σ_{xx} maxima at higher carrier densities move diagonally in the $E - n$ plane as the σ_{xx} maximum between the states at $\nu = 0$ and 1. In contrast to this expectation, our experimental results in Figure 2 shows that the σ_{xx} maxima between the states $\nu = 1$ and 2, and between the states $\nu = 3$ and 4 remain almost vertical. Therefore, the quantum capacitance effect due to Landau level gaps at $\nu = 0$ cannot fully account for the observation we made in the experiment.

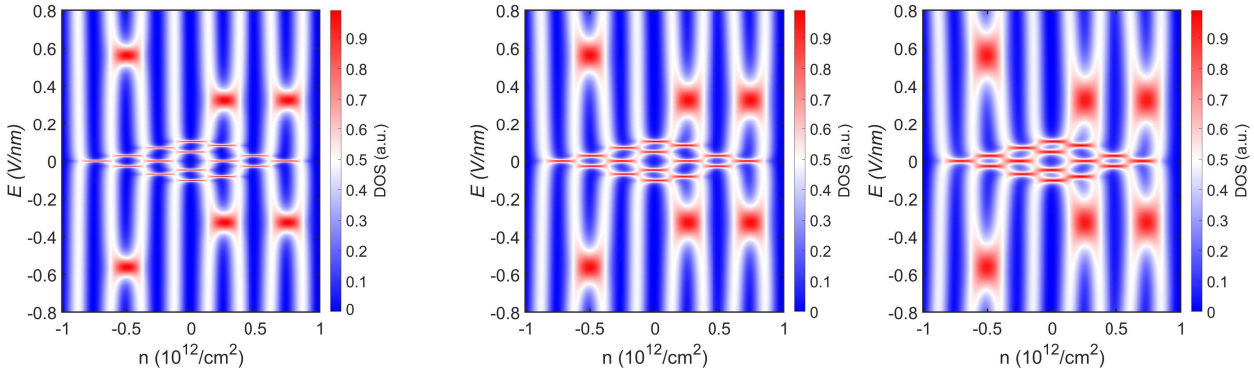

(a) $\gamma = 0.2$ meV (b) $\gamma = 0.35$ meV (c) $\gamma = 0.5$ meV

(d) $\gamma = 0.65$ meV (e) $\gamma = 0.8$ meV

Figure S 4: Colour maps of density of states of the zLL as a function of carrier density and applied electric field field for different disorder strengths or broadening width γ. The model plots for $B_\perp = 10$T, $B_{||} = 0$T include exchange enhanced $g' = 10$ Landé factor and a Lamb shift term $\Delta_L(B_\perp)$ as described in the main text.

II.VIII. Modelling results with different magnetic field configurations

With the optimized model parameters above, we further generate color maps of density of states as a function of carrier density n and transverse electric field E for different perpendicular magnetic fields $B_\perp$ and in-plane magnetic fields $B_{||}$ as shown in Figure S5: (a) $B_\perp = 14$T, $B_{||} = 0$T and (b) $B_\perp = 10$T, $B_{||} = 10$T. These results are used to compare with the experimental data in Figs. 2(b) and 2(c) of the main text, respectively. The model captures the main features of the experimental spectra: increasing $B_\perp$ reduces the value of $|E|$ where the $\nu = -2$ crossing occur, while this value is increased as we increase $B_{||}$.

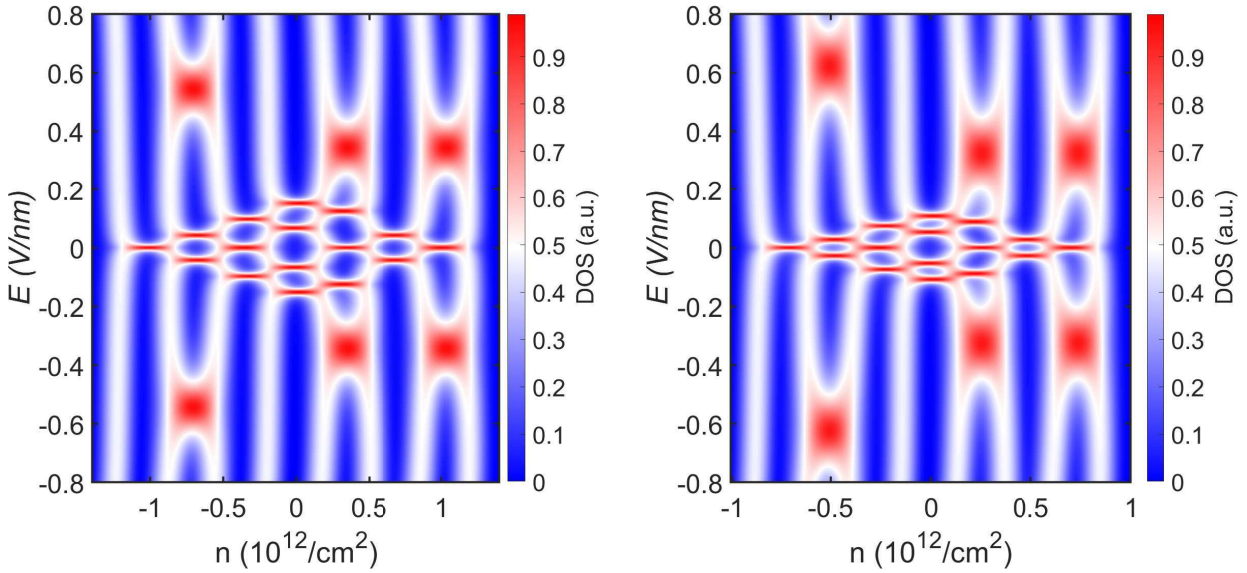

(a) $B_\perp = 14\text{T}, B_{||} = 0\text{T}$ (b) $B_\perp = 10\text{T}, B_{||} = 10\text{T}$

Figure S 5: Colour maps of density of states of the zLL as a function of carrier density and applied electric field for other magnetic field configurations. The model plots include exchange enhanced $g' = 10$ Landé factor and a Lamb shift term $\Delta_L(B_\perp)$ as described in the main text. The broadening width γ used for these plots is 0.5 meV similar to Figure 4(c) and (f) of the main text.

II.IX. Modelling results for previous models

In this section we extend two models used in previous works,[5,6] which successfully explain the intra-zLL crossings at low electric fields, to high electric fields and compare them with our experimental data and theoretical model.

Model 1

This model is from Ref. 5, where they introduce a purely phenomenological model to understand the zLL crossings at low E, especially the $\nu = 0$ crossings. They refer to their model as a skeleton for building an effective single particle like diagram to understand the

zLL crossings. The zero LL energy equations based on their model are as follows -

$$E_{l,v,s} = \frac{1}{2}\xi\Delta_v + \frac{1}{2}\sigma\Delta_B + \frac{1}{2}(2N+\xi)\Delta_l \tag{11}$$

where $\Delta_v = 0.13E + 0.6B$ and ξ denotes the corresponding sign of the valley, $\Delta_s = 1.7B$ and σ denotes the corresponding sign of the spin, and $\Delta_l = 0.058(\sqrt{E} - 9.43)B$ for $E \geq 96$mV/nm and $N = 0, 1$ orbitals. All the energies are in meV, electric field (E) in mV/nm and magnetic field in T. So, using these equations, if we plot the zero LL energy spectrum for high E, we

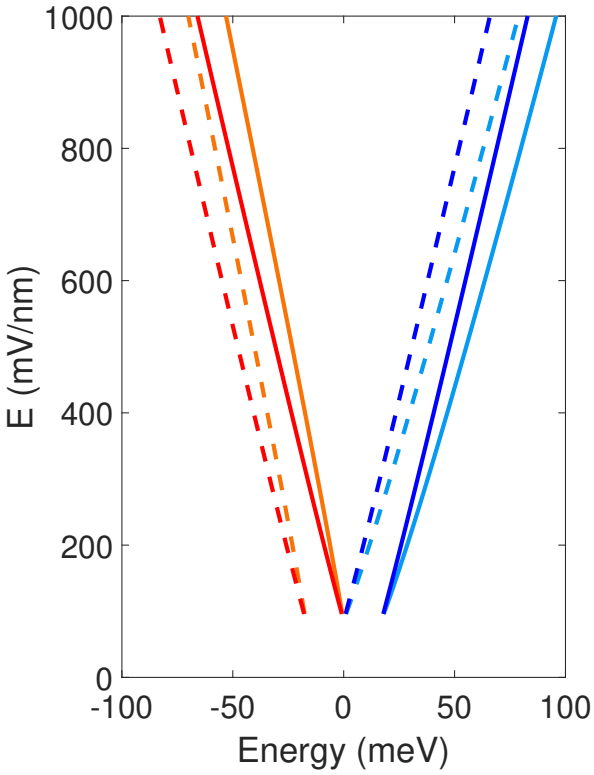

Figure S 6: zero LL energy spectrum based on model discussed using eq.11 The model plots for $B_\perp = 10$T, $B_{||} = 0$T and $E \geq 96$mV/nm. The color code is same as used in Fig. 4 of the main text of our paper.

get that the electron and hole side are symmetric and the $\nu = -2$ crossing can't be observed until 1000mV/nm for $B_\perp = 10$T as shown in Fig. S6 .

Model 2

This model is from Ref. 6, which provides a detailed model including coulomb interactions for the capacitance measurements done on zero-energy LL in bilayer graphene at low E. Extending the model in Ref. 6, we find the relevant phase boundaries for high E crossings -

$$u_*(T_{-2>}) = \frac{2}{1-\alpha_1}\left(-\zeta - \Delta_{Lamb} - \Delta_{10} + \frac{E_C \epsilon^{||}_{BN}}{4\epsilon^{\perp}_{BLG}}\frac{d}{l_B}(4-(1+\alpha_1)^2) + E_Z\right) \tag{12}$$

$$u_*(T_{+1>}) = \frac{2}{1-\alpha_1}\left(-\zeta - \Delta_{Lamb} + \Delta_{10} + \frac{E_C \epsilon^{||}_{BN}}{4\epsilon^{\perp}_{BLG}}\frac{d}{l_B}3(1-\alpha_1^2)\right) \tag{13}$$

$$u_*(T_{+2>}) = \frac{2}{1-\alpha_1}\left(-\zeta - \Delta_{Lamb} + \Delta_{10} + \frac{E_C \epsilon^{||}_{BN}}{4\epsilon^{\perp}_{BLG}}\frac{d}{l_B}(4-(1+\alpha_1)^2) + E_Z\right) \tag{14}$$

$$u_*(T_{+3>}) = \frac{2}{1-\alpha_1}\left(-\zeta - \Delta_{Lamb} + \Delta_{10} + \frac{E_C \epsilon^{||}_{BN}}{4\epsilon^{\perp}_{BLG}}\frac{d}{l_B}(1-\alpha_1^2)\right) \tag{15}$$

In these expressions, $u_*(T_{\nu>})$ means the interlayer bias potential in meV where the phase transition (T) happens for filling factor ν at higher electric fields ($>$ sign represents the crossing at higher E). As specified earlier, the interlayer bias potential u is related to electric field E by $u = CE$, where $C = 121$ meVnm/V for this model. The model parameters used are all listed in Table 2.

In order to compare the similarities and differences between Model 2 and our modelling results, we have plotted Model 2's zLL as a function of carrier density and electric field for different magnetic field configurations in Fig. S7 and compared with our model in Table 3 for high E and Table 4 for low E. With regards to similarities, Model 2's zLL crossing values, as well as their evolution under different magnetic field configurations align well with our experimental (Fig. 2) and modeling results for both low and high E on the hole side as well as for low E on the electron side. And in the case of differences, Model 2 predicts zLL $\nu = 1$ and 3 high E crossings at ≈ 4 times higher electric field values (Fig. S7) than our modeling

Table 2: Model 2 parameters for zLL crossings

Model Parameters	Description
α_1	$(1 - .012B_\perp)$, where $B_\perp$ is in Tesla
d	Spacing between BLG layers $(0.334nm)$
l_B	Magnetic length $(26B_\perp^{-0.5}\text{nm})$
$\epsilon_{BLG}^{\perp}$	$(2.76\epsilon_0)$ Electric permittivity of BLG
$\epsilon_{BN}^{\parallel}$	$(6.6\epsilon_0)$ Electric permittivity of BN
E_Z	Zeeman spin splitting energy $(0.11B_{total}$ in meV)
Δ_{10}	Single particle orbital splitting energy $(0.313B_\perp$ in meV)
E_C	Bare screening potential energy $(8.58B_\perp^{0.5}$ in meV)
$\hbar\omega_c$	Cyclotron energy $(2.58B_\perp$ in meV)
a_{scr}	Screening strength $(0.5E_C/\hbar\omega_c)$
Δ_{Lamb}	Lamb-shift Energy term (-$0.2E_C/(1 + 2.73a_{scr})$in meV)
ζ	Exchange Energy term(-$0.315E_C/(1 + 2.52a_{scr})$in meV)

Table 3: Comparison of Model 2 zLL crossings at high E with our modelling results. Here, $T_{\nu>}$ means the phase transition (T) happening at filling factor ν at higher electric fields ($>$ sign represents the crossing at higher E).

Name of Transition	Magnetic field $(B_\perp, B_{\|})$	zLL crossings value from Model 2 (V/nm)	zLL crossings value from Our model (V/nm)
$T_{-2>}$	(10,0) T	0.58	0.56
	(14,0) T	0.534	0.54
	(10,10) T	0.64	0.62
$T_{+1>}$	(10,0) T	1.31	0.326
	(14,0) T	1.27	0.344
	(10,10) T	1.31	0.326
$T_{+3>}$	(10,0) T	1.26	0.326
	(14,0) T	1.21	0.344
	(10,10) T	1.26	0.326
$T_{+2>}$	(10,0) T	1.44	1.21
	(14,0) T	1.40	1.23
	(10,10) T	1.50	1.27

results. In addition, these crossings decrease slightly with increasing $B_\perp$, contrary to both our experimental (Fig. 2) and modeling results. This shows that despite of the similarities of both models at low E, these models behave differently at high E, which suggests that even a detailed model like Model 2 utilizing multiple fitting parameters needs some modifications to explain the zLL crossings at high electric fields.

Finally, we noted that both the models predict intra-zLL crossings at $\nu = 2$ for electric

Table 4: Comparison of Model 2 zLL crossings at low E with our modelling results. Here, $T_{\nu<}$ means the phase transition (T) happening at filling factor ν at lower electric fields ($<$ / $>$ sign represents the crossing at lower/higher E).

Name of Transition	Magnetic field $(B_\perp, B_{\|})$	zLL crossings value from Model 2 (V/nm)	zLL crossings value from Our model (V/nm)
$T_{-2<}$	(10,0) T	0.005	0.028
	(14,0) T	0.011	0.042
	(10,10) T	0.005	0.028
$T_{+1<}$	(10,0) T	0.07	0.082
	(14,0) T	0.099	0.12
	(10,10) T	0.074	0.088
T_{-1}	(10,0) T	0.067	0.069
	(14,0) T	0.092	0.097
	(10,10) T	0.07	0.074
$T_{0<}$	(10,0) T	0.06	0.047
	(14,0) T	0.079	0.066
	(10,10) T	0.064	0.052
$T_{0>}$	(10,0) T	0.076	0.103
	(14,0) T	0.11	0.15
	(10,10) T	0.08	0.108

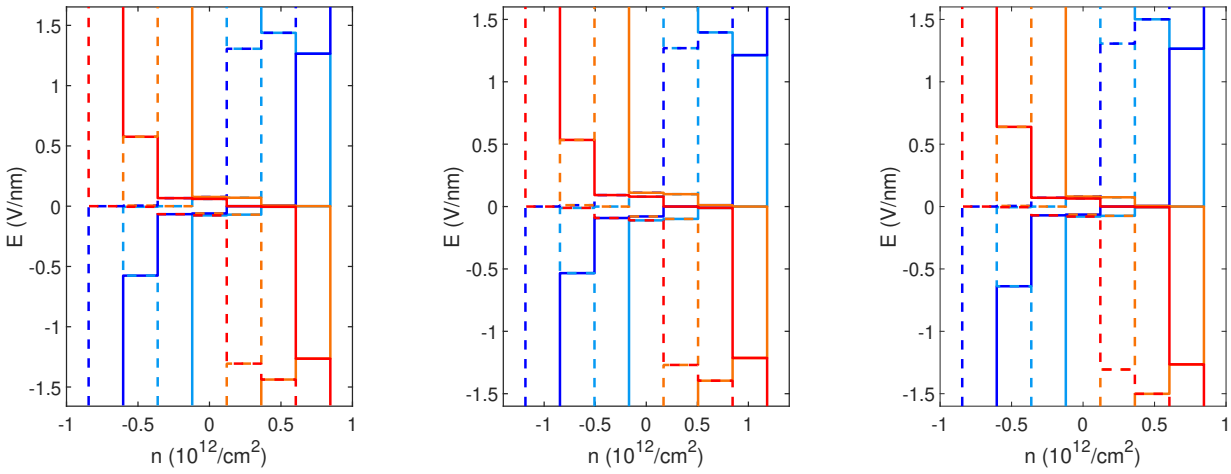

(a) $B_\perp = 10$T,$B_{||} = 0$T (b) $B_\perp = 14$T,$B_{||} = 0$T (c) $B_\perp = 10$T,$B_{||} = 10$T

Figure S 7: zLL energies plots as a function carrier density (n) vs Electric Field (E) based on Model 2 calculations, extending for large electric field to highlight the newly observed phase transitions. The model plots are for different magnetic field configurations as specified. The color code is same as used in Fig. 4 of the main text of our paper.

fields beyond the range of our measurements (Fig. S7). This would be an interesting observation for future works to further refine our understanding of BLG zLL under higher electric fields.

References

(1) Wang, L.; Meric, I.; Huang, P. Y.; Gao, Q.; Gao, Y.; Tran, H.; Taniguchi, T.; Watanabe, K.; Campos, L. M.; Muller, D. A.; Guo, J.; Kim, P.; Hone, J.; Shepard, K. L.; Dean, C. R. One-Dimensional Electrical Contact to a Two-Dimensional Material. *Science* **2013**, *342*, 614–617.

(2) Purdie, D. G.; Pugno, N. M.; Taniguchi, T.; Watanabe, K.; Ferrari, A. C.; Lombardo, A. Cleaning interfaces in layered materials heterostructures. *Nature Communications* **2018**, *9*, 5387.

(3) Huang, Y.; Sutter, E.; Shi, N. N.; Zheng, J.; Yang, T.; Englund, D.; Gao, H.-J.; Sutter, P. Reliable Exfoliation of Large-Area High-Quality Flakes of Graphene and Other Two-Dimensional Materials. *ACS Nano* **2015**, *9*, 10612–10620, PMID: 26336975.

(4) McCann, E.; Koshino, M. The electronic properties of bilayer graphene. *Reports on Progress in Physics* **2013**, *76*, 056503.

(5) Li, J.; Tupikov, Y.; Watanabe, K.; Taniguchi, T.; Zhu, J. Effective Landau Level Diagram of Bilayer Graphene. *Phys. Rev. Lett.* **2018**, *120*, 047701.

(6) Hunt, B. M.; Li, J. I. A.; Zibrov, A. A.; Wang, L.; Taniguchi, T.; Watanabe, K.; Hone, J.; Dean, C. R.; Zaletel, M.; Ashoori, R. C.; Young, A. F. Direct measurement of discrete valley and orbital quantum numbers in bilayer graphene. *Nature Communications* **2017**, *8*, 948.

(7) McCann, E.; Fal'ko, V. I. Landau-Level Degeneracy and Quantum Hall Effect in a Graphite Bilayer. *Phys. Rev. Lett.* **2006**, *96*, 086805.

(8) Pan, C.; Wu, Y.; Cheng, B.; Che, S.; Taniguchi, T.; Watanabe, K.; Lau, C. N.; Bockrath, M. Layer Polarizability and Easy-Axis Quantum Hall Ferromagnetism in Bilayer Graphene. *Nano Letters* **2017**, *17*, 3416–3420.

(9) Shizuya, K. Structure and the Lamb-shift-like quantum splitting of the pseudo-zero-mode Landau levels in bilayer graphene. *Phys. Rev. B* **2012**, *86*, 045431.

(10) Lamb, W. E.; Retherford, R. C. Fine Structure of the Hydrogen Atom by a Microwave Method. *Phys. Rev.* **1947**, *72*, 241–243.

(11) Velasco, J.; Jing, L.; Bao, W.; Lee, Y.; Kratz, P.; Aji, V.; Bockrath, M.; Lau, C. N.; Varma, C.; Stillwell, R.; Smirnov, D.; Zhang, F.; Jung, J.; MacDonald, A. H. Transport spectroscopy of symmetry-broken insulating states in bilayer graphene. *Nature Nanotechnology* **2012**, *7*, 156–160.

(12) Maher, P.; Dean, C. R.; Young, A. F.; Taniguchi, T.; Watanabe, K.; Shepard, K. L.; Hone, J.; Kim, P. Evidence for a spin phase transition at charge neutrality in bilayer graphene. *Nature Physics* **2013**, *9*, 154–158.

(13) Lee, K.; Fallahazad, B.; Xue, J.; Dillen, D. C.; Kim, K.; Taniguchi, T.; Watanabe, K.; Tutuc, E. Chemical potential and quantum Hall ferromagnetism in bilayer graphene. *Science* **2014**, *345*, 58–61.

(14) Zhang, Y.; Tang, T.-T.; Girit, C.; Hao, Z.; Martin, M. C.; Zettl, A.; Crommie, M. F.; Shen, Y. R.; Wang, F. Direct observation of a widely tunable bandgap in bilayer graphene. *Nature* **2009**, *459*, 820–823.

(15) Weitz, R. T.; Allen, M. T.; Feldman, B. E.; Martin, J.; Yacoby, A. Broken-Symmetry States in Doubly Gated Suspended Bilayer Graphene. *Science* **2010**, *330*, 812–816.

(16) Kim, S.; Jo, I.; Dillen, D. C.; Ferrer, D. A.; Fallahazad, B.; Yao, Z.; Banerjee, S. K.; Tutuc, E. Direct Measurement of the Fermi Energy in Graphene Using a Double-Layer Heterostructure. *Phys. Rev. Lett.* **2012**, *108*, 116404.

(17) Yu, G. L.; Jalil, R.; Belle, B.; Mayorov, A. S.; Blake, P.; Schedin, F.; Morozov, S. V.; Ponomarenko, L. A.; Chiappini, F.; Wiedmann, S.; Zeitler, U.; Katsnelson, M. I.; Geim, A. K.; Novoselov, K. S.; Elias, D. C. Interaction phenomena in graphene seen through quantum capacitance. *Proceedings of the National Academy of Sciences* **2013**, *110*, 3282–3286.